ACS Catalysis

Research Article

pubs.acs.org/acscatalysis

Visible Light Driven Photoelectrochemical Water Oxidation by Zn- and Ti-Doped Hematite Nanostructures

Naghmehalsadat Mirbagheri,[†,‡,⊥] Degao Wang,[§,⊥] Cheng Peng,*[,§] Jianqiang Wang,[§] Qing Huang,[§] Chunhai Fan,[§] and Elena E. Ferapontova*[,†]

[†]Interdisciplinary Nanoscience Center and [‡]Sino-Danish Centre for Education and Research (SDC), Aarhus University, Gustav Wieds Vej 1590-14, DK-8000 Aarhus C, Denmark

[§]Division of Physical Biology, Bioimaging Center, Shanghai Synchrotron Radiation Facility, CAS Key Laboratory of Interfacial Physics and Technology, Shanghai Institute of Applied Physics, Chinese Academy of Sciences, Shanghai 201800, China

Supporting Information

ABSTRACT: The electrodeposition method was used for modification of a nanostructured hematite photoanode with Ti and Zn to improve the photoelectrocatalytic performance of hematite in the water splitting reaction. The photoelectrocatalytic activity of the hematite electrodes modified with Ti^{4+} and Zn^{2+} was optimized through the controlled variation of the dopant ion concentration in the electrodeposition solution. Under optimized conditions, for standard illumination of AM 1.5G (100 mW cm^{-2}), the photocurrent density at the Ti/Zn-modified hematite anode reached 1.5 mA cm^{-2} at 1.23 V vs RHE that was 2.5-times higher than that observed with the pristine hematite electrode, the photoelectrocatalysis onset potential being 63 mV reduced. Effects of Ti and Zn doping on the photoelectrochemical activity of pristine hematite were studied by scanning electron microscopy, UV−vis spectroscopy, elemental analysis, and electrochemical impedance spectroscopy. On the basis of the obtained results, the improved performance of the Ti/Zn-modified hematite stemmed from the combination of the enhanced electrical conductivity along with the facilitated charge transport in the bulk phase and at the surface of hematite. The effect of Zn-doping decreasing the overpotential of the reaction by 218 mV (solely Zn-doped compared to that of the pristine hematite) was correlated with the Zn contribution to the interfacial catalysis of water oxidation.

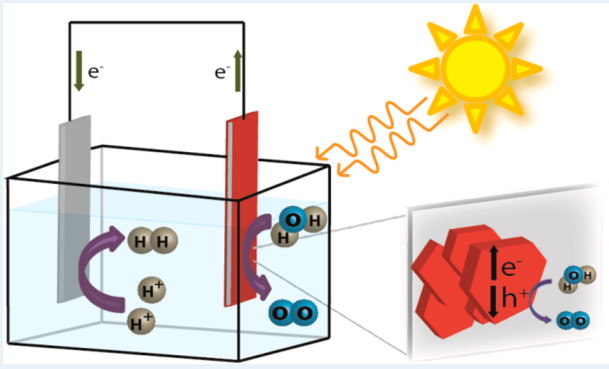

KEYWORDS: *photoelectrocatalysis, water oxidation reaction, α-Fe_2O_3 (hematite), Ti-doped hematite, Zn-doped hematite, solar energy conversion*

1. INTRODUCTION

A large portion of total world energy consumption is derived from such fossil fuels as natural gas, oil, and coal. However, the fossil fuel reserves are nonrenewable, and their combustion is environmentally hazardous. Therefore, replacing this source of energy by such reproducible and harmless energy resources as solar energy has been drawing more attention than ever before.[1,2] In this context, the energy available from sunlight can be harvested in a photovoltaic device (PV), where it may be either directly converted to electrical energy or captured in a photoelectrochemical cell (PEC) device and then, through such chemical reactions as a water splitting reaction, be stored in the form of molecular hydrogen (clean fuel in fuel cells).[3−5]

Numerous semiconductors such as TiO_2,[6] $BiVO_4$,[7] WO_3,[8] and α-Fe_2O_3 (hematite)[9] have been used as photoanodes in PEC systems for solar energy conversion operating via the water splitting reaction. Recent studies have indicated that hematite is one of the most promising photoanodes due to its high stability in alkaline and neutral electrolytes, low cost, nontoxicity, and narrow band gap of around 1.9 to 2.2 eV (depending on the method of the hematite preparation), which enables it to reach a solar to hydrogen transformation efficiency up to 16.8% under AM 1.5G illumination.[9] Though hematite has a suitable valence band position for the water oxidation reaction, the position of its conduction band is lower than the hydrogen reduction potential; therefore, additional electrical bias is required to achieve the water reduction reaction by solar radiation. In addition, hematite suffers from intrinsically poor conductivity,[10] low absorption coefficient,[11] low carrier mobility (<1 cm^2 V^{-1} s^{-1}),[12] very short excited-state lifetime (~10 ps),[12,13] and short hole-diffusion length (~2 to 4 nm),[14] which significantly limit the intrinsic hematite quantum efficiency and therefore reduce its photoelectrocatalytic activity.

Received: October 16, 2013
Revised: May 7, 2014
Published: May 8, 2014

Various strategies such as incorporation of impurities,[15,16] morphological nanomaterial manipulation of size and form,[17−20] surface treatments,[21] and some other approaches[22,23] have been probed with the hematite photoanode to overcome these problems. Incorporation of different elements as dopants into the hematite structure to make it either an n-type[12,15,24] or p-type[25] semiconductor can improve the catalytic activity of this photoelectrode and modification of the hematite surface with iridium[26] or cobalt[27,28] catalysts was reported to greatly reduce the photocurrent onset potential and therefore increase the water splitting efficiency. Thus, several attempts have been made to improve the performance of this system, but it is clear that more investigations are necessary to develop an efficient photoelectrode and make it technologically applicable in the large-scale production world.

In this work, we aimed at the improvement of the catalytic activity of hematite by modifying hematite electrodes with Ti^{4+} and Zn^{2+} by the electrodeposition method (Table S1, Supporting Information) and studying the photoelectrocatalysis of water oxidation by the modified electrodes. Several research groups have reported that incorporation of each of these ions into hematite could significantly improve the hematite photoelectrocatalytic activity in the water splitting reaction through various mechanisms. For example, the enhanced photoactivity of Ti-modified hematite electrodes was assigned to the enhancement of the electrical conductivity and carrier concentration,[12,29] improvement of charge-transfer rate coefficient at the surface,[10] passivation of surface states resulting in the decrease of the electron−hole recombination rate,[12,30] and resurrection of the dead surface.[31] For hematite modified with Zn^{2+}, however, the increased flat-band potential at the semiconductor−electrolyte junction[21,32] passivation of the surface defects[21] and enhancement of the electron−hole separation at the hematite interface[33] were discussed as the reasons for the higher photoactivity of the Zn^{2+}-treated hematite electrode as compared to that of pristine hematite. Therefore, to take advantage of both Ti and Zn, we investigated the deposition of these ions within hematite in order to achieve a higher photoelectrocatalytic activity and efficiency of the Fe_2O_3 photoanode in the water splitting reaction, namely, the low onset potential of photoelectrocatalysis and higher plateau currents. Structural, electrical, and optical analysis was performed to study the role of Ti and Zn in the performance of the modified electrodes.

2. EXPERIMENTAL SECTION

2.1. Materials. Titanium(IV) chloride ($TiCl_4$), zinc(II) chloride ($ZnCl_2$), ferric chloride ($FeCl_3{\cdot}6H_2O$), hydrogen peroxide 30% (H_2O_2), potassium chloride (KCl), and potassium fluoride (KF) were all of A.R. grade and were purchased from Sinopharm Chemical Reagent Co. Ltd. in Shanghai. All aqueous solutions were prepared with deionized (DI) water from Milli-Q-Water (Millipore Corp, 18.2 MΩ/cm at 25 °C). Fluorine-doped tin oxide coated glass (FTO, TEC-15) was purchased from Nippon Sheet Glass, Japan.

2.2. Preparation of Hematite Electrodes. Electrodeposition of hematite was carried out using a standard three-electrode cell. FTO was the working electrode, Ag/AgCl (saturated KCl) was the reference electrode, and a platinum wire served as the counter electrode. Before electrodeposition, the FTO electrodes were cleaned ultrasonically in pure water, ethanol, acetone, and finally rinsed in water again. Then, the cleaned FTO electrodes were immersed into the electrodeposition solution containing 5 mM $FeCl_3$, 5 mM KF, 0.1 M KCl, and 1 M H_2O_2.[34] For modification of hematite with zinc (Zn-modified hematite electrode) or titanium (Ti-modified hematite electrode), calculated amounts of $ZnCl_2$ or $TiCl_4$ were added to the electrodeposition solution to achieve the Zn molar ratio, [Zn]/([Zn] + [Fe]), of 5.66, 10.71, and 16.67% and the Ti molar ratio, [Ti]/([Ti] + [Fe]), of 0.99, 1.38, 1.96, and 3.10%. For the modification of hematite with both titanium and zinc (Ti/Zn-modified hematite electrode), a mixed solution of Ti and Zn with a Ti molar ratio, [Ti]/([Ti] + [Zn] + [Fe]), of 1.23, 1.40, 1.85, and 1.92% and a Zn molar ratio, [Zn]/([Ti] + [Zn] + [Fe]), of 1.92, 5.56, 5.58, and 10.58% was added to the electrodeposition solution. These molar ratios were used in the first part of the work (section 3.1) to identify the samples. Deposition of the hematite film was performed by applying 100 potential cycles between −0.2 to 0.4 V vs Ag/AgCl at a scan rate of 200 mV s^{-1} and 50 °C. After electrodeposition, the hematite-modified FTO electrode was thoroughly rinsed with Milli-Q water and then dried at room temperature. The obtained yellowish film was annealed at 800 °C for 10 min in an air atmosphere.

2.3. Characterization Techniques. Elemental analysis was performed using an ICP-OES spectrometer (SPECTRO ARCOS) to determine the molar ratio % of elements in the electrodeposited films (Table S2, Supporting Information). The morphology of samples was characterized by SEM (JME2011, JEOL, Japan). UV−vis absorption spectra were collected by a Hitachi U-3010 spectrophotometer (Hitachi, Japan) and Raman spectra by a confocal Raman microscope (HORIBA, Japan). X-ray diffraction (XRD) spectra were carried out with an X-ray diffractometer (Bruker AXS, D8 Advanced) using Cu Kα radiation (λ = 1.5418 Å), and X-ray photoelectron spectra (XPS) were recorded using two instruments: (1) a PerkinElmer 1257 model, operating at an average base pressure of ∼5.9 × 10^{-9} Torr at 300 K with a nonmonochromatized Al Kα line at 1486.6 eV, and a hemispherical sector analyzer capable of 25 meV resolution; and (2) a Kratos Axis Ultra DLD instrument (Kratos Analytical Ltd., Telford, UK) equipped with a monochromated Al Kα X-ray source ($h\nu$ = 1486.6 eV) operating at 15 kV and 10 mA (150 W). Survey spectra (binding energy (BE) range of 0−1200 eV with a pass energy of 160 eV) were used for element identification and quantification. The acquired data were converted to the VAMAS format and analyzed using CasaXPS (Casa Software Ltd., UK) software. Voltammetry and electrochemical impedance spectroscopy (EIS) were performed by an Autolab electrochemical workstation (Metrohm AG, Switzerland) equipped with a Nova 1.8 software.

2.4. Photoelectrochemical Studies. The hematite photoanode was prepared by sealing a part of the hematite-covered FTO electrode (including the edges) with epoxy resin except for the 0.15 cm^2 unsealed area left for photoexcitation experiments; an external Cu wire contact to the FTO substrate was fabricated by soldering the wire to the FTO surface using a 63/37 Sn/Pb solder. All photoelectrochemical measurements were performed at 23 ± 3 °C in a three-electrode quartz PEC connected to a potentiostat CHI650B (Chenhua company, Shanghai) equipped with CHI650B electrochemical analyzer software, with the Pt counter electrode, the Ag/AgCl (saturated KCl) reference electrode, and a hematite photoanode as the working electrode. Experiments were performed in deaerated 1 M NaOH aqueous solutions at pH 13.6. A xenon lamp (300 W, Perfect Light Corp. Ltd. Beijing) with an infrared filter

dx.doi.org/10.1021/cs500372v | ACS Catal. 2014, 4, 2006−2015

(absorbance ≥780 nm) was used as the illumination source directly radiating on the surface of the photoanode placed in the quartz photoelectrochemical cell. The radiation intensity at the working electrode was measured without the IR filter as 100 mW cm^{-2} by a solar power meter (TES-1333, ZhongXuan Electronic Corp. Ltd., Shanghai). In a typical experiment, the photoanode was immersed into the quartz PEC and illuminated under simulated sunlight initiated from the xenon lamp. Photocurrent measurements were performed in the dark and under illumination (AM 1.5G, 100 mW cm^{-2}) conditions by using linear sweep voltammetry (LSV) at a scan rate of 10 mV s^{-1} and EIS with a sinusoidal perturbation amplitude of 10 mV, performed within the 100 kHz to 0.1 Hz frequency range. The potentials obtained vs Ag/AgCl were converted to the reversible hydrogen electrode (RHE) scale according to the Nernst equation:

$$E_{RHE} = E_{Ag/AgCl} + 0.059\ pH + E^0_{Ag/AgCl} \quad (1)$$

where E_{RHE} is the converted potential vs RHE, $E^0_{Ag/AgCl}$ is 0.1976 V at 25 °C, and $E_{Ag/AgCl}$ is the experimentally measured potential vs Ag/AgCl reference electrode. For the solution pH used (pH 13.6), eq 1 reduces to eq 2:

$$E_{RHE} = E_{Ag/AgCl} + 1 \quad (2)$$

which was used all over the work for the conversion of $E_{Ag/AgCl}$ to E_{RHE}.

The incident photon to current conversion efficiency (IPCE) experiments with the hematite samples were performed in 1 M NaOH electrolyte at 1.23 V vs RHE using a solar simulator (Newport 66902, 500 W xenon lamp) coupled to a monochromator (Newport 74125). The IPCE as a function of the wavelength was calculated according to the following equation:[35]

$$IPCE = \frac{1240 \times j_{ph}}{\lambda \times j_{phD}/R_\lambda} = \eta_{ext} \times \frac{j_{ph}}{j_{phD}} \quad (3)$$

where λ is the wavelength of incident light (nm), R_λ is the responsivity of the Si photodetector (Newport 71675) provided by the supplier (A W^{1-}), η_{ext} is the external quantum efficiency of the Si photodetector, and j_{phD} is the photocurrent density at the Si photodetector (mA cm^{-2}). The photocurrent density for the hematite photoanode j_{ph} was calculated as follows:[35]

$$j_{ph} = \frac{I_{ph} - I_d}{A_{ph}} \quad (4)$$

where I_{ph} and I_d are the currents measured under illumination and in the dark, respectively (mA), and A_{ph} is the light spot size (cm^2).

3. RESULTS AND DISCUSSION

3.1. Photoelectrocatalytic Activity of Hematite Electrodes in the Water Splitting Reaction. The performance of the pristine hematite and hematite electrodes modified with Ti, Zn, and both elements in combination were investigated by LSV. The recorded photocurrents were evaluated with respect to the photoelectrocatalysis onset potential and photocurrent density observed at the thermodynamic potential of the water oxidation reaction (1.23 V vs RHE). The photoelectrocatalytic activity of Ti-modified hematite was dramatically improved compared to that of the pristine hematite. While the current density of around 2×10^{-3} mA cm^{-2}, detected at 1.23 V for the pristine hematite electrode in the dark, increased drastically up to 0.59 mA cm^{-2} under light illumination, a further enhancement of the photocurrent was achieved with the Ti-modified hematite electrodes (Figure S1A, Supporting Information). The maximum photocurrent density was exhibited by the 1.96% Ti-modified hematite electrode, which was approximately two times higher than that observed with the pristine hematite. In addition, this sample showed an 83 mV lower photocurrent onset potential, suggesting more efficient carrier transportation. Along with that, the photocurrent density of the Ti-modified hematite electrodes significantly reduced with a further increasing Ti concentration (curve 5, Figure S1A, Supporting Information), approaching that of the pristine hematite electrodes.

The photoelectrocatalytic performance of the Zn-containing hematite photoanodes relative to the pristine hematite electrode was also interrogated as a function of the varying Zn concentration in the electrodeposition solution (Figure S1B, Supporting Information). In contrast to the Ti-modified samples, a relatively small enhancement of the photoelectrocatalytic currents was observed for the Zn-modified hematite electrodes; however, for 10.71% Zn the onset potential of the water oxidation reaction reduced down to 670 mV vs RHE (around 218 mV decrease), and the higher photocurrent density could be followed. 10.71% Zn was found to be the optimal Zn-dopant concentration, while at a higher concentration of Zn the photocurrent response dropped (curve 4, Figure S1B, Supporting Information).

Finally, a significant enhancement in the photoelectrocatalytic activity of hematite was achieved by altering the Ti and Zn concentrations in the electrodeposition solution, with the maximal photocurrent density attained with the samples prepared from 1.40% Ti + 5.58% Zn-containing solutions (Figure S1C, Supporting Information) that demonstrated a photocurrent density 2.5-fold higher than that of the pristine hematite electrode at 1.23 V vs RHE (1.5 mA cm^{-2}).

Thus, the photoelectrocatalytic activity of the Ti- and Zn-modified hematite photoanodes in the water splitting reaction essentially depended on the concentration of the dopant ions and their relative concentrations (summarized data for pristine hematite and best performing Zn-, Ti-, and Ti/Zn-modified hematite electrodes are shown in Figure 1). A similar performance was also obtained with these electrodes under the constant-potential measurements at 1.4 V vs RHE (the photocurrent stability profile is shown in Figure S2, Supporting Information). The variation in the photoelectrocatalytic performance of the Ti- and Zn-modified hematite photoanodes raises the following questions: (A) How do Ti and Zn improve the photocurrent density of the hematite electrode? (B) Why does the Zn-modified hematite electrode shift the photocurrent onset potential to less positive potentials? (C) Why was the best photoelectrocatalytic performance observed with the 1.40% Ti + 5.58% Zn-modified hematite electrode? To address these questions and find out the role Ti and Zn play in the improvement of the photoelectrocatalytic activity of hematite electrodes prepared by electrodeposition, we performed a detailed structural and electrochemical analysis of the best performing samples (10.71% Zn-, 1.96% Ti-, and 1.40% Ti + 5.58% Zn-modified hematite electrodes, which are further referred to as Zn-, Ti-, and Ti/Zn-modified hematite electrodes, respectively).

dx.doi.org/10.1021/cs500372v | ACS Catal. 2014, 4, 2006−2015

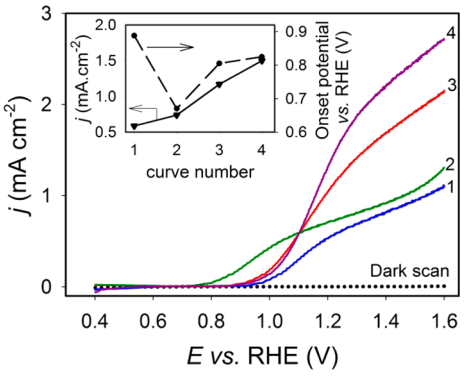

Figure 1. Representative current−potential curves in the dark (dotted line) and under simulated illumination (solid curves) recorded for (1) pristine hematite, (2) 10.71% Zn, (3) 1.96% Ti, and (4) 1.40% Ti + 5.58% Zn-modified hematite electrodes. Inset: the photocurrent onset potential (dashed line) and current density (solid line) at 1.23 V vs RHE for the hematite and modified-hematite electrodes.

3.2. SEM Analysis of the Surface Structure of Hematite Samples. SEM analysis of the hematite samples showed that the electrodeposited hematite films were not uniform and consisted of crystalline pine nut-like nanostructures of submicrometer (100−200 nm) size (Figure 2). The electrodeposited film was composed of two main parts, a thin sublayer of about 100 nm and a layer with agglomerated deposited nanoparticles of different size well sintered to each other (Figure 2B). Although all samples have a very similar morphology, a slight growth in the particle size for the modified hematite samples was observed, which might be due to the increasing mass resulting from the incorporation of Ti and/or Zn within the hematite structure (Figure 2D−F).

3.3. XRD Analysis of the Pristine and Modified Hematite Samples. To characterize the crystalline structure of the produced films, the XRD spectra of the pristine and modified hematite thin films were recorded (Figure 3A). Generally, the obtained XRD patterns are dominated by the diffraction peaks characteristic of the fluorine-doped SnO_2 under layer (Figure 3A, peaks labeled with asterisks). Along with that, the characteristic hematite XRD peaks were also observed for all samples corresponding to the (012), (104), (110), (113), (024), (116), (214), and (300) hematite planes, with the most intense (110) peak. The relatively high intensity of the latter designates a strong preferential orientation of the [110] axis vertical to the substrate. This preferred orientation of (110) thus may contribute to the improved electron transport along that axis (vertically through the film) due to the higher conductivity of this plane relative to the other planes in hematite.[36] Other crystal structures of Zn, Ti, and their hybrid oxide with Fe were not detected in the obtained XRD patterns of these samples.[37,38]

3.4. Raman Spectroscopic Characterization of Hematite Films. Composition of the formed hematite films was characterized by Raman spectroscopy (Figure 3B). Seven optical modes (2Ag + 5Eg) are possible for α-Fe_2O_3 in its Raman spectrum, and five of those modes that correspond to Ag, 223 and 496 cm^{-1}, and Eg, 290, 406, and 609 cm^{-1}, are detectable.[39] An extra peak seen in Figure 3B at approximately 657 cm^{-1} can be tentatively assigned to the presence of either magnetite (Fe_3O_4), maghemite (γ-Fe_2O_3), or wustite (FeO).[39] Since FeO is not so stable at room temperature[40] (particularly, at high annealing temperatures in the presence of air oxygen) and the other obtained Raman peaks are inconsistent with the γ-Fe_2O_3 spectrum,[39] we assume that this peak may refer to magnetite (Fe_3O_4), which has been reported to be presumably formed in the course of electrodeposition of the hematite films.[41,42] For the pristine hematite, the ratio of this peak at 657 cm^{-1} to the Fe_2O_3 peak at 609 cm^{-1} was around 0.47, and higher ratios of the 657/609 cm^{-1} peaks were observed for the modified hematite samples, especially for Ti/Zn-modified hematite (Figure 3B, inset). That may be discussed either in terms of changes in the oxygen stoichiometry upon replacement of Fe^{3+} in the hematite lattice by Ti^{4+} or possible changes in the Fe^{3+} to Fe^{2+} stoichiometry that might ensure the electroneutrality of the lattice upon Fe^{3+} substitution by Ti^{4+}.[10,43] Both may be considered as contributing to the enhancement of the electronic conductivity of the modified

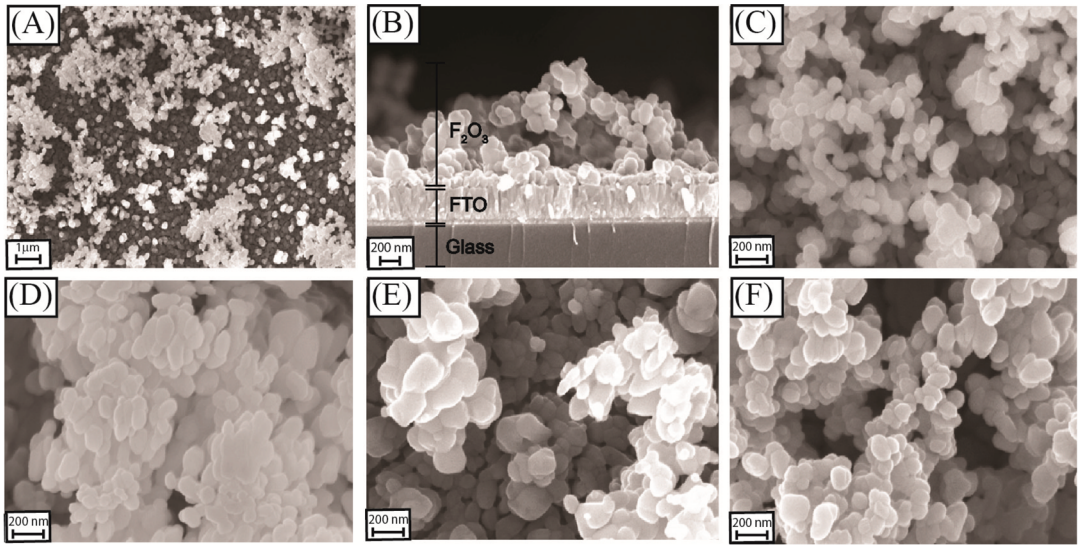

Figure 2. Representative SEM images of the electrodeposited (A−C) pristine hematite and (D−F) modified hematite: (A) 1 μm-scale top view, (B) cross-sectional view, (C) 200 nm-scale top view of the pristine hematite, and 200 nm-scale top view of the (D) Zn-, (E) Ti-, and (F) Ti/Zn-modified hematite electrodes.

dx.doi.org/10.1021/cs500372v | ACS Catal. 2014, 4, 2006−2015

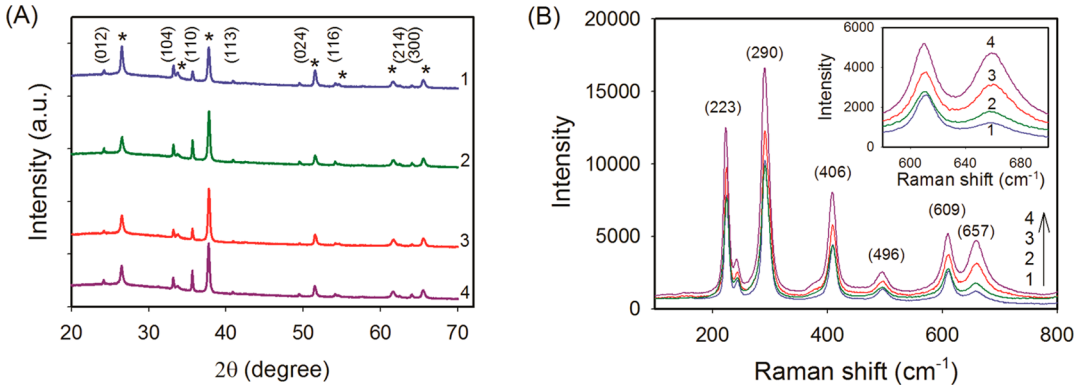

Figure 3. Representative (A) X-ray diffraction patterns and (B) Raman spectra of the (1) pristine hematite, (2) Zn-, (3) Ti-, and (4) Ti/Zn-modified hematite sample. The diffraction peaks of SnO_2 indicated by * originate from the FTO substrate.

hematite samples and, therefore, to their improved photoelectrocatalytic performance.

3.5. XPS Analysis of the Surface Composition of Hematite Films. The hematite surface elemental composition and the component chemical states were analyzed by XPS (Figure S3, Supporting Information). Two characteristic bands of Fe^{3+} at about 711 eV (Fe $2p_{3/2}$) and 725 eV (Fe $2p_{1/2}$) accompanied by their satellites at the high binding energy side (about 8 eV)[44] were detected for all samples (Figure S3A, Supporting Information). The presence of Fe^{2+} within the hematite structure was not supported by XPS. No signal corresponding to the presence of this ion in any of the studied samples was detected, in line with other reports,[45−48] where the absence of this signal has been ascribed, among other reasons, to delocalization of the Fe^{2+}extra electron over several Fe cations in such a way that the average extent of reduced Fe appears to be negligible and undetectable by XPS. The O 1s signal was also detected as a broad asymmetric curve composed of two peaks at about 529 and 531 eV (Figure S3B, Supporting Information). The peak at 529 eV is characteristic of oxygen present in the hematite samples, and the peak at 531 eV was attributed to the absorbed hydroxyl groups on the hematite surface.[49]

Signals from Sn^{4+}, resulting from the migration of tin from the underlying FTO to the hematite surface proceeding at high sintering temperature (800 °C),[16] found to be optimal for the photoelectrode preparation, were also distinguishable in all samples (Figure S3C, Supporting Information). Incorporation of this ion, acting as electron-donating substitution impurities,[16] into the hematite lattice was suggested to lead to partial reduction of Fe^{3+} to Fe^{2+} to maintain electroneutrality; as we have discussed earlier, changes in the oxygen stoichiometry cannot be excluded as well. Therefore, such unexpected incorporation of tin can enhance the electrical conductivity of the hematite samples, which, in its turn, may result in higher photoelectrocatalytic activity of the material.[16,50] Since under our annealing conditions Sn was found in all samples, we considered that its effect on photoelectrocatalysis was the same for all samples and that pristine hematite might serve as a reference sample for the analysis of the effects of Zn and Ti.

As displayed in Figure S3D, Supporting Information, Ti signals at around 458 eV (Ti $2p_{3/2}$) and 464 eV (Ti $2p_{1/2}$) can be clearly observed in the Ti- and Ti/Zn-modified hematite samples. These binding energies are consistent with fully oxidized titanium (Ti^{4+}),[43,49] while no Ti signals were detected both in pristine and solely Zn-modified hematite (curves 1 and 2 in Figure S3D, Supporting Information). In Zn^{2+}-containing samples, Zn^{2+} 2p signals[21] were detected at about 1022 eV (Zn $2p_{3/2}$) and 1045 eV (Zn $2p_{1/2}$) (Figure S3E, Supporting Information) in the Zn- and Ti/Zn-modified hematite samples.

3.6. UV−Vis Spectroscopy Characterization and Band Gap Analysis. UV−vis spectra of the pristine and modified hematite samples showed insignificant differences in the absorbance, very likely due to the variations in the morphology and thickness of the films (Figure S4A, Supporting Information). The absorbance peaks at about 410 and 530 nm, observed for all samples, were attributed to the ligand field transition $3e_{g\uparrow} \rightarrow 3e_{g\downarrow}$ and $6A_1 \rightarrow 4E$ for the high energy absorption as well as interlevel transitions for the lower energy peaks.[51] The optical band gaps of the hematite samples were calculated from the intersection points of the slopes of the both branches of the transition region in the Tauc plots (Figure S4B and C, Supporting Information).[52] In this plot, the band gap energy is calculated using the following relationship:[52]

$$\alpha h\nu \sim (h\nu - E_g)^n \tag{5}$$

where E_g is the separation between the bottom of the conduction band and the top of the valence band, α is the absorption coefficient of the thin film, h is Planck's constant (eV s), ν is the frequency of light (s^{-1}), and n is assumed to be 1/2 and 2 for direct allowed and indirect allowed transitions, respectively.

Although the indirect band gap in hematite in the range of 1.9−2.2 eV has been mostly reported,[14,53,54] there are recent reports on the direct band gap in hematite, related to the quantum size-effect[55] and some cases of hematite preparation by electrodeposition.[24,43] The absorption data of the pristine and modified hematite samples were fitted to the direct (Figure S4B, Supporting Information) and indirect allowed transition conditions (Figure S4C, Supporting Information) with the band gap values of 2.14 and 2.06 eV, respectively. As both pristine and doped hematite samples showed the same band gap values, modification of hematite with Ti, Zn, and both of them was concluded to produce insignificant influence on the band gap characteristic of pristine hematite.

3.7. Mott−Schottky Analysis of the Semiconductor Properties of Pristine and Modified Hematite. To understand which way Ti, Zn, and a combination of these two elements can affect the photoelectrode/electrolyte interfacial properties, the Mott−Schottky analysis of the hematite samples was carried out at 1000 Hz and in the dark.

dx.doi.org/10.1021/cs500372v | ACS Catal. 2014, 4, 2006−2015

The Mott–Schottky analysis is based on the following equation:[56]

$$1/C^2 = \left(\frac{2}{q\varepsilon\varepsilon_0 N_D}\right)\left(E - E_{FB} - \frac{kT}{q}\right) \quad (6)$$

where C is the space charge capacitance (F), q is the electron charge (C), ε is the hematite dielectric constant of 80,[57] ε_0 is the dielectric permittivity of vacuum (F m^{-1}), N_D is the carrier density (cm^{-3}), E is the electrode potential applied (V), E_{FB} is the flat band potential (V), k is the Boltzmann's constant, and T is the temperature (the value of kT/q is 0.026 V at 25 °C).[58] In the ideal case, the C^{-2} vs E dependence is linear, and the plot may be used to estimate a flat band potential (E_{FB}) and carrier density (N_D) in semiconductors, from the intercept of the plot with the Y-axis at $C^{-2} = 0$ and the slope of the Mott–Schottky dependence, respectively, while the depletion layer width (ω) of the semiconductor is calculated according to the following equation:[59]

$$\omega = \left[(2\varepsilon\varepsilon_0/qN_D)\left(E - E_{FB} - \frac{kT}{q}\right)\right]^{1/2} \quad (7)$$

eq 6 is generally valid for (1) zero resistance of metal or electrolyte and bulk semiconductor phases; (2) a barrier with perfectly blocking properties; (3) low/zero concentration of surface states; (4) the absence of interfacial layers, such as an insulating layer in the semiconductor/metal case or a Helmholtz layer in the semiconductor/electrolyte; and (5) perfectly planar and two-dimensionally infinite interfaces, and some other restriction conditions.[60] Since most of these conditions are not sufficiently addressed in real experimental cases, plots of C^{2-} vs E may not be linear.[12,61] For our hematite samples, a fair linearity of the Mott–Schottky plots was observed within the potential range from 0.7 to 1.3 V vs RHE (Figure 4, inset), and these linear parts were used to estimate the flat band potential and carrier density.

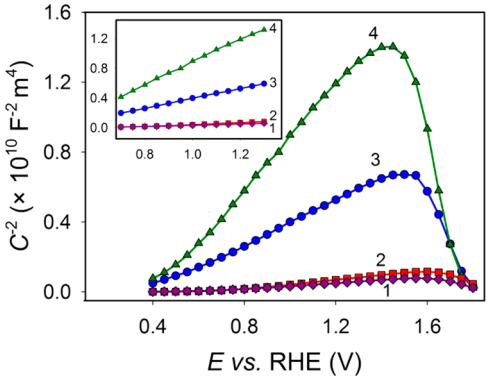

Figure 4. Representative Mott–Schottky plots for the (1) Ti/Zn-, (2) Ti-, (3) pristine hematite, and (4) Zn-modified hematite electrodes. Inset: linear parts of the plots used for analysis. The axis titles in the inset are the same as those in the main figure.

Table 1 summarizes the calculated values of the carrier density, depletion layer width, flat band potential, and photocurrent density for the studied electrodes. The depletion layer widths of the samples were calculated from the capacitance values at 1.23 V vs RHE.

The positive slopes of the Mott–Schottky dependences observed for all electrodes indicate that the pristine and modified hematite samples belong to the n-type semiconductors, in agreement with the majority of the reports.[15,21,24,33] The Ti-modified hematite has a carrier concentration of 1.40 × 10^{21} cm^{-3}, which is more than 5-fold higher than that of pristine hematite. Enhancement of the electron concentration in the Ti-doped hematite can be attributed to the substitution of Fe^{3+} by Ti^{4+} in the hematite lattice, resulting, as was earlier discussed, either in the possible changes in the oxygen stoichiometry or in the formation of Fe^{2+} sites, to maintain the charge balance in the lattice. Such charge redistribution may apparently improve the electron transfer properties and therefore the conductivity of the sample, at the expense of extra electrons generated in the system.[10,62] Although Ti acts as an n-type dopant and one should expect a flat band potential more negative than that of the pristine hematite,[29] a less negative flat band potential was observed for the Ti-doped hematite. This behavior was previously described by Jin and co-workers.[12] In the case of the Zn-doped hematite, the lower carrier concentration and the same flat band potential as that of the pristine hematite were obtained. Therefore, the improved photoelectrocatalytic performance of this sample cannot be attributed to the favorable changes in the carrier density and flat band potential.[33,48] However, a better charge separation due to the increased width of the space–charge region estimated for the Zn-doped hematite may be responsible for the improved photoelectrocatalytic activity of the Zn-modified hematite electrode as compared to that of the pristine hematite. The Ti/Zn-modified hematite sample has a more positive flat band potential value. However, the highest concentration of charge carriers in this sample may be the most important contribution to the highest (among all other samples) increase in the photocurrent density.

Table 1. Semiconductor Properties of the Pristine and Modified Hematite Electrodes

sample	N_D (cm^{-3})	ω (Å)	E_{FB} (V vs RHE)	photocurrent density at 1.23 (V vs RHE)
Zn-modified hematite	1.16 × 10^{20}	79.4	0.39	0.74
pristine hematite	2.66 × 10^{20}	52.9	0.38	0.59
Ti-modified hematite	1.40 × 10^{21}	19.5	0.63	1.17
Ti/Zn-modified hematite	2.13 × 10^{21}	16.5	0.57	1.51

3.8. Photoconversion Efficiency of the Samples. The IPCE analysis of the modified hematite samples preformed at different wavelengths indicated a significantly improved performance of doped compared to pristine hematite (Figure 5), consistent with the obtained photoelectrochemical responses. At 400 nm, the maximum IPCE achieved for the Ti/Zn-modified hematite sample was around 2.5-fold higher than that of the pristine hematite. Consistent with the previously reported results,[24,36] a large enhancement of the IPCE was observed at low wavelengths for all samples, which can be ascribed to the enhancement of charge separation efficiency in the outermost layers of the hematite samples.

3.9. EIS Analysis of Pristine and Modified Hematite Electrodes. To further understand the effect of Ti and Zn doping on the charge transfer properties of hematite, the EIS analysis of the modified hematite electrodes was accomplished. The Nyquist plots were obtained for selected samples in the dark and under one sun simulation conditions, at the applied

dx.doi.org/10.1021/cs500372v | ACS Catal. 2014, 4, 2006–2015

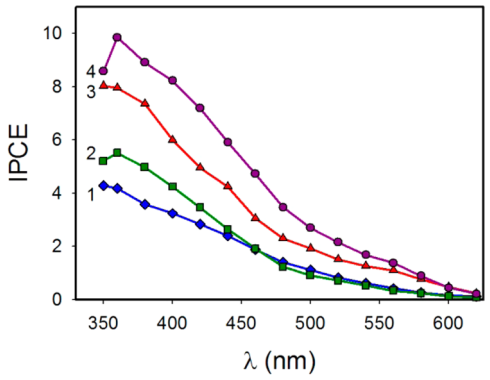

Figure 5. IPCE dependence on the wavelength for (1) pristine hematite, (2) Zn-, (3) Ti-, and (4) Ti/Zn-modified hematite electrodes.

potential of 1 V vs RHE (Figure 6C and D, respectively). In the dark, one semicircle was observed for all samples, which fitted well to a simple Randles circuit composed of the resistance of the electrochemical cell, R_{cell}, and charge transfer resistance at the hematite electrode−electrolyte interface, $R_{ct,s}$, in series, and the space−charge capacitance at the electrode surface, $C_{sc,s}$, in parallel to the $R_{ct,s}$ (Figure 6A).[63] Under simulated sunlight illumination, two distinct semicircles were detected, consistent with the equivalent circuit represented in Figure 6B and including the R_{cell}, the charge transfer resistance, $R_{ct,b}$, and the space−charge capacitance, $C_{sc,b}$, of the bulk hematite, as well as the Helmholtz capacitance at the hematite electrode−electrolyte interface, C_H, and the charge transfer resistance at the hematite electrode−electrolyte interface, $R_{ct,s}$.[64] As the electronic process in the bulk of a semiconductor is much faster compared to the process at the semiconductor−electrolyte interface, the high frequency impedance response may be correlated with the $R_{ct,b}$ and the $C_{sc,b}$, while in the low frequency region, the EIS signal is predominantly due to the contribution from the $R_{ct,s}$ and the C_H.[49,64]

The equivalent circuit parameters estimated by fitting the impedance data to the corresponding equivalent circuits are summarized in Table 2. As can be seen, the resistance values obtained in the dark are much higher than those obtained under illumination. Thus, switching from the dark to sunlight illumination conditions substantially decreases the charge transfer resistance, which may be correlated with the higher charge carrier mobility in the presence of sunlight. In addition, all modified hematite samples showed resistance lower than that of the pristine hematite, consistent with the improved electrical conductivity of hematite upon modification (Table 2). Therewith, the lowest capacitance was observed with the Zn-doped hematite electrode, while the Ti/Zn-doped hematite electrode showed the largest capacitance value, in agreement

Table 2. Charge Transfer Resistance and Capacitance Values Estimated by Fitting the EIS Data to the Corresponding Equivalent Circuits Represented in Figure 6A and B

	dark conditions		under illumination			
sample	$R_{ct,s}$[a] (Ω)	$C_{sc,s}$[b] (μF)	$R_{ct,b}$[c] (Ω)	$C_{sc,b}$[d] (μF)	$R_{ct,s}$[a] (Ω)	C_H[e] (μF)
pristine hematite	453 × 10^3	2.85	651	1.37	1.91 × 10^3	12.0
Zn-modified hematite	448 × 10^3	2.08	571	1.27	1.39 × 10^3	10.0
Ti-modified hematite	327 × 10^3	5.98	211	3.10	1.70 × 10^3	35.4
Ti/Zn-modified hematite	247 × 10^3	9.37	159	6.18	1.01 × 10^3	66.9

[a]Charge transfer resistance at the electrode−electrolyte interface. [b]Space−charge capacitance at the electrode surface. [c]Charge transfer resistance of the bulk hematite. [d]Space−charge capacitance of the bulk hematite. [e]Helmholtz layer capacitance.

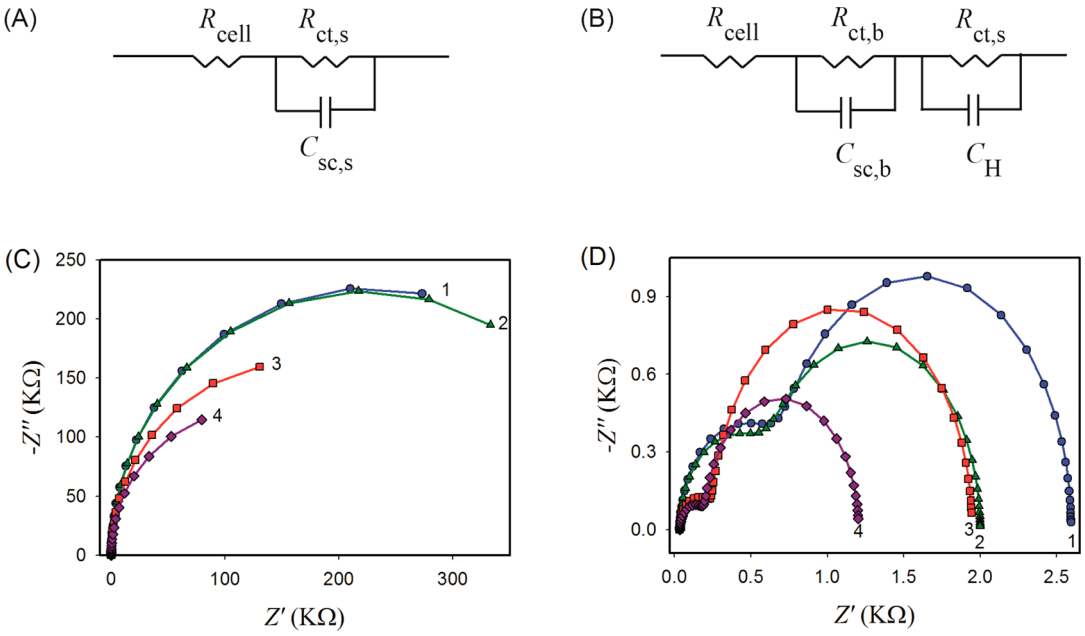

Figure 6. Equivalent circuit used to fit EIS data measured (A) in the dark and (B) under illumination. Representative Nyquist plots measured at 1 V vs RHE for (1) pristine hematite, (2) Zn-, (3) Ti-, and (4) Ti/Zn-modified hematite electrodes recorded (C) in the dark and (D) under illumination.

dx.doi.org/10.1021/cs500372v | ACS Catal. 2014, 4, 2006−2015

with the Mott–Schottky data obtained at 1 V vs RHE (Figure 4).

The change in the $C_{sc,b}$ was consistent with the estimated depletion layer width values (Table 1): the capacitance decreased with the increasing depletion layer width. Moreover, the capacitance values obtained under illumination indicate that for all samples the C_H values were essentially larger than the $C_{sc,b}$ values (Table 2), correlating with a thicker space–charge region at the semiconductor–electrolyte interface.[65]

While the Ti^{4+} dopant effect could be related to the improved charged transport properties of the hematite matrix, in agreement with other reports on the effect of similar and higher charge dopant elements[15,24,41] exhibited in the increased photocurrent densities, the role of Zn-doping, shifting the reaction onset potential to 218 mV less positive, was not completely clear. Since in some works the improved water oxidation potentials, e.g., for Co-modified hematite, were ascribed either to the changes in surface states of the modified hematite sample,[28] or, in the case of Zn-doping, to the formation of the ultrathin electron-blocking ZnO layer,[21] to investigate the role of Zn on the surface states, the EIS data obtained under illumination were also fitted to the equivalent circuit represented in in Figure S5A, Supporting Information. The equivalent circuit elements included the space–charge capacitance of the bulk hematite ($C_{sc,b}$), the surface state capacitance (C_{ss}), the resistance of trapping of holes in the surface state (R_{trap}), and the charge transfer resistance from the surface state to solution ($R_{ct,ss}$).[31,66] The obtained capacitance and resistance values represented in Table 3 are very similar to

Table 3. Capacitance and Resistance Values Estimated by Fitting the EIS Data to the Corresponding Equivalent Circuit Represented in Figure S5A, Supporting Information

	under illumination			
sample	R_{trap}[a] (Ω)	$C_{sc,b}$[b] (μF)	$R_{ct,ss}$[c] (Ω)	C_{ss}[d] (μF)
pristine hematite	805	1.23	1.75×10^3	11.8
Zn-modified hematite	720	1.13	1.24×10^3	10.0
Ti-modified hematite	250	2.85	1.66×10^3	33.3
Ti/Zn-modified hematite	190	5.66	978	63.2

[a]The resistance of the trapping of holes in the surface state. [b]The space–charge capacitance of the bulk. [c]The charge transfer resistance from the surface state to solution. [d]The surface state capacitance.

our previous data (Table 2, under illumination). In comparison to the pristine hematite, the lower $R_{ct,ss}$ and lower C_{ss} values were observed for the Zn-doped hematite electrode. This is consistent with the faster charge transfer from the surface states in the Zn-doped hematite compared to that of the pristine hematite, which leads to a lower hole concentration at the surface of the Zn-doped hematite and thus to a lower capacitance. This suggests that Zn as a dopant accelerates the charge transfer kinetics and can be considered as an interfacial catalyst for the improvement of the water oxidation onset potential.[28]

3.10. Effect of Zn Doping of Hematite on Photoelectrocatalysis of Water Oxidation. The reduced overpotential of the water oxidation reaction observed at the Zn-doped hematite electrodes can be correlated rather with the improved interfacial catalysis of the reaction than with the improved charge transport (as in the case of Ti-doping), affecting the photocurrent densities at a given potential rather than the onset potential. Several reasons for that can be considered, including a quite generalized Zn effect on the surface states of hematite.

In general, the mechanism of the photoelectrocatalytic oxidation of water (or hydroxide anions, in basic solutions) on hematite electrodes is not yet well understood.[67] For interfacial water (hydroxide), oxidation, generated by light holes (eq 8), should be collected in the space charge region and then transferred to the interface to the surface associated reactants, e.g., a hematite lattice oxygen atom or an iron atom as represented below:[68]

$$h\nu \rightarrow h^+ + e^- \quad (8)$$

$$Fe(III)_{surf} + h^+ \rightarrow Fe(IV)_{surf} \quad (9a)$$

$$Fe(IV) + e^- \rightarrow Fe(III) \quad (9b)$$

$$Fe(IV)_{surf} + h^+ \rightarrow Fe(V)_{surf} \quad (9c)$$

$$Fe(V) + e^- \rightarrow Fe(IV) \quad (9d)$$

$$2Fe(V)_{surf} + 4OH^- \rightarrow 2Fe(III) + O_2 + 2H_2O \quad (10)$$

In n-type semiconductors such as hematite, the hole transfer resulting in water (hydroxide) oxidation competes with the surface (alternatively, space–charge region) recombination of holes and electrons at the surface hole-trapping states (eqs 9b and 9d),[68] the whole process depending on the potential applied and the balance between the surface mediated charge-recombination and charged transfer rate constants.[69] Since the detailed mechanism of the water oxidation reaction on hematite is quite complex, its general evaluation based on the experimentally measured Tafel slopes may be proposed to reveal the Zn effect on interfacial catalysis (Figure 7).

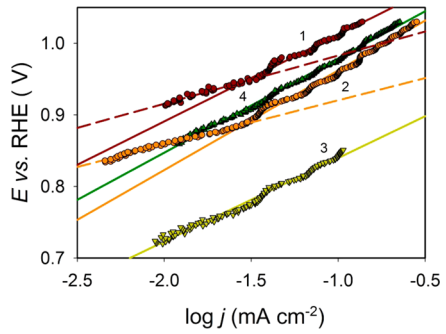

Figure 7. Apparent Tafel plots constructed for (1) hematite, (2) Ti-doped hematite, (3) Zn-doped hematite, and (4) Ti/Zn-doped hematite electrodes. Other conditions are identical to those in Figure 1. The Tafel slopes are (1) 67 ± 3 and 121 ± 2 mV/decade; (2) 62 ± 1 and 139 ± 1 mV/decade; (3) 117 ± 1 mV/decade; and (4) 132 ± 1 mV/decade.

In the presence of Zn, the apparent Tafel slopes for the photoelectrocatalytic oxidation of water at the Zn- and Ti/Zn-doped hematite electrodes approached 120 mV per decade, characteristic of a metallized semiconductor with a high concentration of surface states,[70] while for pristine and solely Ti-doped hematites they were close to 59 mV/decade, characteristic of a semiconductor with a low concentration of surface states (though transforming into 120 mV/decade with increasing positive potential)[71] (Figure 7, curves 1 and 2). These data point to the contribution of Zn to the surface-

dx.doi.org/10.1021/cs500372v | ACS Catal. 2014, 4, 2006–2015

associated catalysis of water oxidation, possibly by decreasing the rate of surface-mediated electron−hole recombination. Similar effects of Co and Al, reflected in the decreased overpotential of the reaction but quite a small change in the photocurrent density, have been already discussed in the context of the role of surface states.[28,66] Thus, the shift in the photoelectrocatalysis onset potential in the presence of Zn (Figure 1) may be associated with the Zn effect on the electrode surface catalytic process since for the improved surface electrocatalytic process along with the decrease in the reaction overvoltage, a nearly identical performance of doped and undoped hematite samples is expected at high potentials.[24] Along with that, this process is evidently more complex than that discussed above. In the presence of Ti, photoelectrocatalysis of water oxidation at Ti/Zn-modified hematite electrodes shifts back to the potentials closer to those of prisitine hematite, though with higher photocurrent densities than at solely Ti-doped hematite electrodes, while for the Zn-modified hematite electrodes not only the decrease in the reaction overvoltage but also a certain enhancement in the photocurrent densities (though less pronounced than that observed with Ti-doped electrodes) are observed, implying the corresponding improvement in charged transport properties of the hematite matrix.

4. CONCLUSIONS

In summary, we employed a facile and simple electrodeposition method for the modification of the hematite photoanode with titanium and zinc. The Raman spectroscopy and EIS analysis of the produced pristine and modified hematite samples demonstrated the improvement of electrical conductivity of the hematite electrodes after Ti and/or Zn doping. Successful incorporation of Ti and Zn was confirmed by the XPS analysis. Since no peak corresponding to zinc oxide, titanium dioxide, or their combination with iron was detected in the XRD pattern of the hematite samples modified with Zn and/or Ti, we suggest that Zn and/or Ti are doped as amorphous phase(s) into the structure of the hematite lattice. Ti-doped hematite showed a significant improvement of the photoelectrocatalytic activity (enhanced photocurrents) as a result of the increased charge carrier concentration and electrical conductivity. The improved performance of the Zn-modified hematite electrodes, demonstrating the reduced onset potential of the water oxidation reaction, was most likely due to the Zn contribution to the surface states and acceleration of charge transfer kinetics, by this making Zn-doped hematite an actual water oxidation catalyst. The best photoelectrocatalytic performance of the hematite photoanode was achieved by hematite modification with Ti and Zn (Ti/Zn-modified hematite). The higher carrier concentration was suggested to be the most important reason for the better photoelectrocatalytic activity of the Ti/Zn-modified hematite as compared to that of the pristine and either Ti- or Zn-modified hematite electrodes.

■ ASSOCIATED CONTENT

Supporting Information

Optimization of the dopant level within the photoanode structure, XPS analysis, UV−vis spectra, and band gap determination of the pristine and modified hematite samples. This material is available free of charge via the Internet at http://pubs.acs.org.

■ AUTHOR INFORMATION

Corresponding Authors

*(C.P.) E-mail: pengcheng@sinap.ac.cn.

*(E.E.F.) E-mail: elena.ferapontova@inano.au.dk.

Author Contributions

⊥N.M. and D.W. contributed equally to this work

Notes

The authors declare no competing financial interest.

■ ACKNOWLEDGMENTS

We greatly appreciate Ms. He Suixia's assistance with SEM measurements, Dr. Peter Hald's help with ICP measurments, and John Lundgaard Hansen's assistance with XPS measurements. This work was financially supported by the Sino-Danish Center for Education and Research (SDC) through their support of the research stay of NSM at the Shanghai Institute of Applied Physics, the National Natural Science Foundation 51102272 and 91127001, Foundation of State Key Laboratory of Coal Combustion FSKLCC1209, and the Faculty of Science and Technology, Aarhus University.

■ REFERENCES

(1) Kamat, P. V. *J. Phys. Chem. C* **2007**, *111*, 2834−2860.
(2) Turner, J. A. *Science* **1999**, *285*, 687−689.
(3) Archer, M. D. *Phys. E* **2002**, *14*, 61−64.
(4) Grätzel, M. *Nature* **2001**, *414*, 338−344.
(5) Walter, M. G.; Warren, E. L.; McKone, J. R.; Boettcher, S. W.; Mi, Q. X.; Santori, E. A.; Lewis, N. S. *Chem. Rev.* **2010**, *110*, 6446−6473.
(6) Fujishima, A.; Honda, K. *Nature* **1972**, *238*, 37−38.
(7) Jia, Q. X.; Iwashina, K.; Kudo, A. *Proc. Natl. Acad. Sci. U.S.A.* **2012**, *109*, 11564−11569.
(8) Su, J. Z.; Feng, X. J.; Sloppy, J. D.; Guo, L. J.; Grimes, C. A. *Nano Lett.* **2011**, *11*, 203−208.
(9) Sivula, K.; Le Formal, F.; Grätzel, M. *ChemSusChem* **2011**, *4*, 432−449.
(10) Glasscock, J. A.; Barnes, P. R. F.; Plumb, I. C.; Savvides, N. *J. Phys. Chem. C* **2007**, *111*, 16477−16488.
(11) Itoh, K.; Bockris, J. O. *J. Electrochem. Soc.* **1984**, *131*, 1266−1271.
(12) Franking, R.; Li, L. S.; Lukowski, M. A.; Meng, F.; Tan, Y. Z.; Hamers, R. J.; Jin, S. *Energy Environ. Sci.* **2013**, *6*, 500−512.
(13) Cherepy, N. J.; Liston, D. B.; Lovejoy, J. A.; Deng, H. M.; Zhang, J. Z. *J. Phys. Chem. B* **1998**, *102*, 770−776.
(14) Kennedy, J. H.; Frese, K. W., Jr. *J. Electrochem. Soc.* **1978**, *125*, 709−714.
(15) Sartoretti, C. J.; Alexander, B. D.; Solarska, R.; Rutkowska, W. A.; Augustynski, J.; Cerny, R. *J. Phys. Chem. B* **2005**, *109*, 13685−13692.
(16) Sivula, K.; Zboril, R.; Le Formal, F.; Robert, R.; Weidenkaff, A.; Tucek, J.; Frydrych, J.; Grätzel, M. *J. Am. Chem. Soc.* **2010**, *132*, 7436−7444.
(17) Goncalves, R. H.; Lima, B. H. R.; Leite, E. R. *J. Am. Chem. Soc.* **2011**, *133*, 6012−6019.
(18) Li, L. S.; Yu, Y. H.; Meng, F.; Tan, Y. Z.; Hamers, R. J.; Jin, S. *Nano Lett.* **2012**, *12*, 724−731.
(19) Lin, Y. J.; Yuan, G. B.; Sheehan, S.; Zhou, S.; Wang, D. W. *Energy Environ. Sci.* **2011**, *4*, 4862−4869.
(20) Warren, S. C.; Voitchovsky, K.; Dotan, H.; Leroy, C. M.; Cornuz, M.; Stellacci, F.; Hebert, C.; Rothschild, A.; Grätzel, M. *Nat. Mater.* **2013**, *12*, 842−849.
(21) Xi, L. F.; Bassi, P. S.; Chiam, S. Y.; Mak, W. F.; Tran, P. D.; Barber, J.; Loo, J. S. C.; Wong, L. H. *Nanoscale* **2012**, *4*, 4430−4433.
(22) Wang, P.; Wang, D. G.; Lin, J.; Li, X. L.; Peng, C.; Gao, X. Y.; Huang, Q.; Wang, J. Q.; Xu, H. J.; Fan, C. H. *ACS Appl. Mater. Interfaces* **2012**, *4*, 2295−2302.

(23) Morrish, R.; Rahman, M.; MacElroy, J. M. D.; Wolden, C. A. *ChemSusChem* **2011**, *4*, 474−479.
(24) Kleiman-Shwarsctein, A.; Hu, Y. S.; Forman, A. J.; Stucky, G. D.; McFarland, E. W. *J. Phys. Chem. C* **2008**, *112*, 15900−15907.
(25) Ingler, W. B.; Baltrus, J. P.; Khan, S. U. M. *J. Am. Chem. Soc.* **2004**, *126*, 10238−10239.
(26) Tilley, S. D.; Cornuz, M.; Sivula, K.; Grätzel, M. *Angew. Chem., Int. Ed.* **2010**, *49*, 6405−6408.
(27) Barroso, M.; Cowan, A. J.; Pendlebury, S. R.; Grätzel, M.; Klug, D. R.; Durrant, J. R. *J. Am. Chem. Soc.* **2011**, *133*, 14868−14871.
(28) Riha, S. C.; Klahr, B. M.; Tyo, E. C.; Seifert, S.; Vajda, S.; Pellin, M. J.; Hamann, T. W.; Martinson, A. B. F. *ACS Nano* **2013**, *7*, 2396−2405.
(29) Meng, X. Y.; Qin, G. W.; Li, S.; Wen, X. H.; Ren, Y. P.; Pei, W. L.; Zuo, L. *Appl. Phys. Lett.* **2011**, *98*, 112104.
(30) Deng, J. J.; Zhong, J.; Pu, A. W.; Zhang, D.; Li, M.; Sun, X. H.; Lee, S. T. *J. .Appl. Phys.* **2012**, *112*, 084312.
(31) Zandi, O.; Klahr, B. M.; Hamann, T. W. *Energy Environ. Sci.* **2013**, *6*, 634−642.
(32) Kumari, S.; Tripathi, C.; Singh, A. P.; Chauhan, D.; Shrivastav, R.; Dass, S.; Satsangi, V. R. *Curr. Sci.* **2006**, *91*, 1062−1064.
(33) McDonald, K. J.; Choi, K. S. *Chem. Mater.* **2011**, *23*, 4863−4869.
(34) Schrebler, R.; Bello, K.; Vera, F.; Cury, P.; Munoz, E.; del Rio, R.; Meier, H. G.; Cordova, R.; Dalchiele, E. A. *Electrochem. Solid-State Lett.* **2006**, *9*, C110−C113.
(35) Sun, K.; Pang, X. L.; Shen, S. H.; Qian, X. Q.; Cheung, J. S.; Wang, D. L. *Nano Lett.* **2013**, *13*, 2064−2072.
(36) Kay, A.; Cesar, I.; Grätzel, M. *J. Am. Chem. Soc.* **2006**, *128*, 15714−15721.
(37) Chen, S. F.; Zhao, W.; Liu, W.; Zhang, S. J. *Appl. Surf. Sci.* **2008**, *255*, 2478−2484.
(38) Valenzuela, M. A.; Bosch, P.; Jimenez-Becerrill, J.; Quiroz, O.; Paez, A. I. *J. Photochem. Photobiol., A* **2002**, *148*, 177−182.
(39) deFaria, D. L. A.; Silva, S. V.; deOliveira, M. T. *J. Raman. Spectrosc.* **1997**, *28*, 873−878.
(40) Shechter, H.; Hillman, P.; Ron, M. *J. Appl. Phys.* **1966**, *37*, 3043−3047.
(41) Hu, Y. S.; Kleiman-Shwarsctein, A.; Forman, A. J.; Hazen, D.; Park, J. N.; McFarland, E. W. *Chem. Mater.* **2008**, *20*, 3803−3805.
(42) Kumar, P.; Sharma, P.; Solanki, A.; Tripathi, A.; Deva, D.; Shrivastav, R.; Dass, S.; Satsangi, V. R. *Int. J. Hydrogen Energy* **2012**, *37*, 3626−3632.
(43) Zhang, P.; Kleiman-Shwarsctein, A.; Hu, Y. S.; Lefton, J.; Sharma, S.; Forman, A. J.; McFarland, E. *Energy Environ. Sci.* **2011**, *4*, 1020−1028.
(44) McIntyre, N. S.; Zetaruk, D. G. *Anal. Chem.* **1977**, *49*, 1521−1529.
(45) Droubay, T.; Rosso, K. M.; Heald, S. M.; McCready, D. E.; Wang, C. M.; Chambers, S. A. *Phys. Rev. B* **2007**, *75*, 104412.
(46) Hahn, N. T.; Mullins, C. B. *Chem. Mater.* **2010**, *22*, 6474−6482.
(47) Bak, A.; Choi, W.; Park, H. *Appl. Catal., B* **2011**, *110*, 207−215.
(48) Miao, C. H.; Ji, S. L.; Xu, G. P.; Liu, G. D.; Zhang, L. D.; Ye, C. H. *ACS Appl. Mater. Interfaces* **2012**, *4*, 4428−4433.
(49) Wang, G. M.; Ling, Y. C.; Wheeler, D. A.; George, K. E. N.; Horsley, K.; Heske, C.; Zhang, J. Z.; Li, Y. *Nano Lett.* **2011**, *11*, 3503−3509.
(50) Ling, Y. C.; Wang, G. M.; Wheeler, D. A.; Zhang, J. Z.; Li, Y. *Nano Lett.* **2011**, *11*, 2119−2125.
(51) Marusak, L. A.; Messier, R.; White, W. B. *J. Phys. Chem. Solids* **1980**, *41*, 981−984.
(52) Tauc, J.; Menth, A. *J. Non-Cryst. Solids* **1972**, *8−10*, 569−585.
(53) Lian, X. J.; Yang, X.; Liu, S. J.; Xu, Y.; Jiang, C. P.; Chen, J. W.; Wang, R. L. *Appl. Surf. Sci.* **2012**, *258*, 2307−2311.
(54) Kumari, S.; Singh, A. P.; Sonal; Deva, D.; Shrivastav, R.; Dass, S.; Satsangi, V. R. *Int. J. Hydrogen Energy* **2010**, *35*, 3985−3990.
(55) Beermann, N.; Vayssieres, L.; Lindquist, S. E.; Hagfeldt, A. *J. Electrochem. Soc.* **2000**, *147*, 2456−2461.
(56) Bard, A. J.; Faulkner, L. R. *Electrochemical Methods: Fundamentals and Applications*, 2nd ed.; Wiley: New York, 2001; pp 1−833.
(57) Benko, F. A.; Longo, J.; Koffyberg, F. P. *J. Electrochem. Soc.* **1985**, *132*, 609−613.
(58) Xi, L. F.; Chiam, S. Y.; Mak, W. F.; Tran, P. D.; Barber, J.; Loo, S. C. J.; Wong, L. H. *Chem. Sci.* **2013**, *4*, 164−169.
(59) Krol, R. v. d.; Grätzel, M. *Photoelectrochemical Hydrogen Production*; Springer: New York, 2012.
(60) Cardon, F.; Gomes, W. P. *J. Phys. D.: Appl. Phys.* **1978**, *11*, L63−L67.
(61) Fabregat-Santiago, F.; Garcia-belmonte, G.; Mora-Sero, I.; Bisquert, J. *Phys. Chem. Chem. Phys.* **2011**, 9083−9118.
(62) Morin, F. J. *Phys. Rev.* **1951**, *83*, 1005−1010.
(63) Dotan, H.; Sivula, K.; Grätzel, M.; Rothschild, A.; Warren, S. C. *Energy Environ. Sci.* **2011**, *4*, 958−964.
(64) Le Formal, F.; Tetreault, N.; Cornuz, M.; Moehl, T.; Grätzel, M.; Sivula, K. *Chem. Sci.* **2011**, *2*, 737−743.
(65) Wielant, J.; Goossens, V.; Hausbrand, R.; Terryn, H. *Electrochim. Acta* **2007**, *52*, 7617−7625.
(66) Klahr, B.; Gimenez, S.; Fabregat-Santiago, F.; Hamann, T.; Bisquert, J. *J. Am. Chem. Soc.* **2012**, *134*, 4294−4302.
(67) Katz, M. J.; Riha, S. C.; Jeong, N. C.; Martinson, A. B. F.; Farha, O. K.; Hupp, J. T. *Coord. Chem. Rev.* **2012**, *256*, 2521−2529.
(68) Wijayantha, K. G. U.; Saremi-Yarahmadi, S.; Peter, L. M. *Phys. Chem. Chem. Phys.* **2011**, *13*, 5264−5270.
(69) Peter, L. M.; Wijayantha, K. G. U.; Tahir, A. A. *Faraday Discuss.* **2012**, *155*, 309−322.
(70) Khan, S. U. M.; Bockris, J. O. M. Fundamental Aspects of Electron Transfer at Interfaces. In *Modern Bioelectrochemistry*; Gutmann, F., Keyzer, H., Eds.; Plenum Press: New York, 1986; pp 1−44.
(71) When the concentration of surface states is low, the relationship between the reaction overpotential and the current approaches the form similar to that in the Butler−Volmer equation, though, since the change in the potential drop at the semiconductor−electrolyte interface occurs inside the semiconductor, the transfer coefficient, α, is absent in the exponential term.